


Coalescence-induced droplet detachment on low-adhesion surfaces: A three-phase system study

Mostafa Moradi, Mohammad Hassan Rahimian,* and Seyed Farshid Chini
School of Mechanical Engineering, College of Engineering, University of Tehran, Tehran, Iran

 (Received 6 December 2018; revised manuscript received 14 February 2019; published 3 June 2019)

Coalescing water droplets on superhydrophobic surfaces can detach from the surface without the aid of any external forces. This self-propelled droplet detachment mechanism is useful in many applications, such as phase change heat transfer enhancement, self-cleaning surfaces, and anti-icing and antidew coatings. In this article, the coalescence-induced droplet jumping in a three-phase system is numerically investigated. The gaps between the surface structures are filled with a liquid that is immiscible with water, e.g., lubricant. A mass-conserving lattice Boltzmann method is implemented to study the effects of several parameters, such as interfacial tensions, droplet size, and surface wettability on the jumping process. The numerical results show that for relatively high values of lubricant-water interfacial tensions and large surface-water contact angles ($>150^\circ$) the water droplets are capable of detaching. The critical droplet size for jumping is also highly dependent on the lubricant-water interfacial properties. The results of this study provide insights into the fluid-fluid and fluid-solid interactions and shed light on the underlying mechanisms involved in the droplet coalescence process on such surfaces.

DOI: [10.1103/PhysRevE.99.063102](https://doi.org/10.1103/PhysRevE.99.063102)

I. INTRODUCTION

Spontaneous removal of microdroplets on low adhesion surfaces due to coalescence has been shown to have several applications, such as in self-cleaning surfaces [1,2], phase change heat transfer enhancement [3–5], antidew [3,6] and anti-icing coatings [7]. According to literature, this phenomenon was first reported by Kollera and Grigull in 1969 [8]. During experiments with mercury droplets, they discovered that upon coalescence, the merged droplet jumps away from the surface.

When two (or more) droplets coalesce, the surface of the liquid reduces. This leads to a decrease in surface energy. This released energy is converted into kinetic energy. During the coalescence process, due to the presence of capillary forces, a liquid bridge starts to form and grow. This results in an oscillatory motion of the droplets. In the absence of a solid surface, this motion is axisymmetric. But when the two droplets are on top of a solid surface the symmetry breaks and the oscillatory motion turns into an upward translational motion. If the translational kinetic energy overcomes the viscous dissipation and surface adhesion, the droplet jumps away from the surface. This phenomenon happens for microscale droplets (ranging from a few microns to few hundred microns) without the aid of any external forces. Since the size of the droplets are much smaller than the capillary length ($R \ll \sqrt{\sigma/\rho g}$), gravity does not play a role in the droplet removal process [6].

Recently, coalescence-induced droplet jumping has been the topic of many published papers [3–7,9,10]. Condensation experiments conducted on superhydrophobic surfaces have shown that for droplet radii in the range of 5 to 150 μm , the droplet detaches from the surface with a characteristic velocity of $U_j \approx 0.2U_{ic}$, where the inertial-capillary velocity is defined

as $U_{ic} = \sqrt{\sigma/\rho r}$ [4,6,9–12,13]. More recent studies have demonstrated that jumping can also occur for nanodroplets [12,14].

Due to the small-scale nature of the coalescence-induced jumping phenomenon, experimental study can be difficult. Numerical simulation is a helpful tool to better understand the underlying mechanism of jumping, and can also be utilized to investigate the effects of various factors such as wetting state, number, position and size of coalescing drops on jumping velocity. In addition to the experiments, several numerical studies have focused on determining the minimum jumping (critical) droplet radius, initial droplet arrangement [15], the effect of air inertia and viscosity [16], surface wettability [17], and surface morphology [18,19].

Liu *et al.* [20] performed two-dimensional (2D) simulations using a Shan-Chen-type lattice Boltzmann method (LBM) to study the jumping process. In their work the substrate roughness is modeled by rectangular pillars and equilibrium contact angle is $\theta^{eq} = 160^\circ$. In a more recent study, Liu and Cheng [19] extended their work to three dimensions (3D). The results show an equivalence between 2D and 3D simulations in terms of jumping mechanism, critical droplet size, and jumping velocity.

Farokhirad *et al.* [21] investigated the effects of micropillars and surface wettability on droplet jumping velocity and height using an LBM developed by Lee and Liu [22]. In their numerical setup, the substrate roughness is modeled by rectangular-shaped pillars similar to Liu *et al.* [20]. They carried out simulations for Ohnesorge numbers in the range of $0.02 < Oh < 0.4$ and $\theta^{eq} = 110^\circ\text{--}160^\circ$. They reported that for a patterned substrate the jumping velocity and height are lower compared to that of a flat substrate. Also the critical contact angle is lower for the pillared substrate, therefore allowing the droplets to depart at a lower contact angle.

Wang *et al.* [15] used a Shan-Chen-type LBM to study multidroplet jumping and the effects of initial droplet arrangement

*Corresponding author: rahimyan@ut.ac.ir

on a flat substrate with a contact angle of 160° . According to their findings, in a concentrated three-droplet system the characteristic jumping velocity is significantly higher ($>50\%$) than the two-droplet system. Although for a spaced arrangement the jumping velocity reduces drastically.

The effects of droplet size mismatch is addressed in the study conducted by Wasserfall *et al.* [23]. Using a volume-of-fluid (VOF) -based method they demonstrated that droplet size mismatch has a significant impact on jumping velocity. They conducted their simulations for a wide range of droplet sizes with contact angles of $\theta^{\text{eq}} = 155^\circ$ and 170° . For small Ohnesorge numbers a maximum jumping velocity of $0.3U_{\text{ic}}$ is achieved, which is higher than previous reports [23].

The possibility of droplet jumping in three-phase systems has not been studied in previous works. In these systems, the spaces between the micropillars are filled with a liquid which is immiscible with water, e.g., lubricant. The aim of the present paper is to investigate the jumping process of droplets on such surfaces, in order to discover under which conditions the merged droplet is capable of detaching from the surface. A 2D multiphase LBM model based on the Allen-Cahn diffuse interface theory is implemented for the numerical simulations.

In the present paper, a recently developed LBM is utilized, which originally was proposed by Geier *et al.* [24] for two-phase flows and was subsequently extended to three-phase fluid systems by Haghani *et al.* [25]. This method is capable of modeling three-phase immiscible flows with high density and viscosity ratios. One of the drawbacks of earlier free-energy based LBM variants such as the one proposed in Ref. [22] is that the mass of the system is not conserved. The new model not only is mass conserving, but it also significantly improves upon the earlier models in terms of computational speed and efficiency [26].

The paper is organized as follows: First the theory and the important parameters in coalescence-induced droplet jumping is presented. Section III describes the numerical method employed to solve the problem. A detailed description of the problem is given in the following section. The results of the simulations are reported in Sec. V, and finally the conclusions are presented in Sec. VI.

II. THEORY

A. Coalescence-induced droplet jumping

In this paper, we denote water droplets, lubricant, air and the solid surface with indices 1, 2, 3, and s , respectively. For a system of two equally sized droplets, coalescing on top of a substrate with zero adhesion, the balance of energy can be written as

$$E_\sigma = E_1 - E_2 = [2(4\pi r^2) - 4\pi R^2]\sigma_{13} = 1/2mU_j^2, \quad (1)$$

where E_σ is the released surface energy due to coalescence, E_1 and E_2 are system surface energies before and after coalescence, respectively. m is the mass of the merged droplet, U_j is the merged droplet jumping velocity immediately after detachment, and σ_{mn} is the interfacial tension between m and n phases. r is the initial droplet radius, and R is the radius of the merged droplet. $R = 2^{1/3}r$ based on the law of conservation of mass. If we neglect the viscous dissipation and assume that all of the available energy is turned into

kinetic energy, one can find that the jumping velocity is equal to $U_j = 1.11\sqrt{\sigma_{13}/\rho r} = 1.11U_{\text{ic}}$ [18]. In reality, the available energy for jumping, E_a is less than the released surface energy, due to the presence of viscous dissipation, E_v , and work of adhesion, E_w [27]:

$$E_a = E_\sigma - E_v - E_w = 1/2mU_j^2. \quad (2)$$

The work of adhesion is the reversible work that has to be expended to separate two surfaces [28]. The work done for separating the droplets from the solid surface per unit area is

$$E_w = \sigma_{13} + \sigma_{s3} - \sigma_{s1}. \quad (3)$$

For a three-phase system where the interpillar spaces are filled with lubricant, work of adhesion per unit area takes the following form:

$$E_w = f_s[\sigma_{13} + \sigma_{s3} - \sigma_{s1}] + (1 - f_s)[\sigma_{13} + \sigma_{23} - \sigma_{12}], \quad (4)$$

where f_s is the solid fraction of substrate. The first and second terms on the right-hand side of Eq. (4) are the work of adhesion at the water droplet-solid interface, and water droplet-lubricant interface, respectively.

The capillary-inertial coalescence timescale is defined by [6]

$$\tau = \sqrt{\frac{\rho r^3}{\sigma_{13}}}. \quad (5)$$

This timescale governs the unsteady motion of droplets. An important dimensionless number that quantifies the relative significance of viscous effects is the Ohnesorge number:

$$\text{Oh} = \frac{\eta}{\sqrt{\rho\sigma_{13}r}}, \quad (6)$$

where η is the dynamic viscosity of the water droplet. The relative effect of gravity is given by the Bond number:

$$\text{Bo} = \frac{\rho g r^2}{\sigma_{13}}. \quad (7)$$

In the capillary-inertial regime the Bond number is very small and therefore the gravity effects can be neglected.

B. Equivalence between 2D and 3D

It has been demonstrated that there is an equivalence between 2D and 3D systems in terms of capillary bridge dynamics in the asymptotic limit of small liquid bridge radii [29,30]. Although since the momentum is scaled with l^2 in 2D and with l^3 in 3D, initially the rate of momentum growth in 2D is faster than that of 3D. But as the length scale of liquid bridge radius reaches the droplet radius ($r_b \approx r$), the rates become similar. Since the latter stages of the coalescence play the most important role in jumping, it can be inferred that the jumping mechanism in 2D is equivalent to the 3D case. Also, an energy balance similar to Sec. II A reveals that the maximum attainable jumping velocity in 2D is $U_{j,2D} = 1.08\sqrt{\sigma_{13}/\rho r}$ which is comparable to the 3D case.

III. NUMERICAL METHOD

A. Interface tracking method

In this paper, an interface tracking method based on the Allen-Cahn model has been used as the numerical method [25]. The interface tracking equation is solved using the LBM.

To distinguish between different components, a phase field variable, ϕ_i is defined where

$$0 \leq \phi_i \leq 1, \quad \sum_i \phi_i = 1; \quad i = 1, 2, 3. \quad (8)$$

The conservative phase field equation for three-component flows can be written as

$$\begin{aligned} & \frac{\partial \phi_i}{\partial t} + \nabla \cdot (\mathbf{u} \phi_i) \\ &= M_i \nabla \cdot \left[\nabla \phi_i - \mathbf{n}_i |\nabla \phi_i|^{\text{eq}} + \frac{1}{3} \sum_{i=1}^3 \mathbf{n}_i |\nabla \phi_i|^{\text{eq}} \right], \end{aligned} \quad (9)$$

where M_i is the mobility of the i th component, $\mathbf{n}_i = \frac{\nabla \phi_i}{|\nabla \phi_i|}$ is the unit vector normal to the interface of component i , and $|\nabla \phi_i|^{\text{eq}}$ is the magnitude of phase field gradient at equilibrium and is given by

$$|\nabla \phi_i|^{\text{eq}} = \frac{4}{\xi} |\phi_i(1 - \phi_i)|, \quad (10)$$

where ξ is the interface thickness. By minimizing the surface free energy, the profile of the interface between components at equilibrium is obtained. The free surface energy for a system of three components in domain Ω is [31]

$$\mathcal{F}(\phi_1, \phi_2, \phi_3) = \int_{\Omega} \left[\frac{12}{\xi} \mathcal{H}(\phi_1, \phi_2, \phi_3) + \sum_{i=1}^3 \frac{3}{8} \xi \gamma_i |\nabla \phi_i|^2 \right] d\Omega, \quad (11)$$

where \mathcal{H} is the bulk free energy and the second term on the right-hand side is the capillary term. The bulk free energy is given by

$$\mathcal{H}(\phi_1, \phi_2, \phi_3) = \sum_{i=1}^3 \frac{\gamma_i}{2} \phi_i^2 (1 - \phi_i)^2, \quad (12)$$

where γ_i are a set of auxiliary coefficients defined as

$$\begin{aligned} \gamma_1 &= \sigma_{12} + \sigma_{13} - \sigma_{23}, \\ \gamma_2 &= \sigma_{12} + \sigma_{23} - \sigma_{13}, \\ \gamma_3 &= \sigma_{13} + \sigma_{23} - \sigma_{12}. \end{aligned} \quad (13)$$

The phase field variable evolution is a function of the chemical potential, μ defined as the derivative of the functional \mathcal{F} :

$$\mu_i = \frac{\partial \mathcal{F}}{\partial \phi_i} = \frac{4\gamma_i}{\xi} \sum_{j \neq i} \left[\frac{1}{\gamma_i} \left(\frac{\partial \mathcal{H}}{\partial \phi_i} - \frac{\partial \mathcal{H}}{\partial \phi_j} \right) \right] - \frac{3}{4} \xi \gamma_i \nabla^2 \phi_i. \quad (14)$$

The coefficient γ_T is given by

$$\frac{3}{\gamma_T} = \frac{1}{\gamma_1} + \frac{1}{\gamma_2} + \frac{1}{\gamma_3}. \quad (15)$$

The free energy expression of Eq. (11) is consistent with diphasic systems and ensures no nonphysical phase apparition when the following is satisfied [31]:

$$\gamma_i > \frac{\gamma_T}{2} > 0; \quad i = 1, 2, 3. \quad (16)$$

B. Interface tracking: LBM formulation

In order to obtain the phase field variables in a three-component system, calculating two of the phase field variables is sufficient. Enforcing mass conservation, the third one can be obtained. The lattice Boltzmann equation (LBE) for tracking the interface between each phase is written as [25,26]

$$\begin{aligned} & h_{\alpha}^i(\mathbf{x} + \mathbf{e}_{\alpha} \delta t, t + \delta t) \\ &= h_{\alpha}^i(\mathbf{x}, t) - \frac{h_{\alpha}^i(\mathbf{x}, t) - \bar{h}_{\alpha}^{i,\text{eq}}(\mathbf{x}, t)}{\tau_{\phi} + 1/2} + F_{\alpha}^{\phi,i}(\mathbf{x}, t), \end{aligned} \quad (17)$$

where h_{α}^i and $\bar{h}_{\alpha}^{i,\text{eq}}$ are the phase field distribution function and the corresponding equilibrium function. τ_{ϕ} is the phase field relaxation time. $\bar{h}_{\alpha}^{i,\text{eq}}$ is given by

$$\bar{h}_{\alpha}^{i,\text{eq}} = h_{\alpha}^{i,\text{eq}} - \frac{1}{2} F_{\alpha}^{\phi,i}; \quad (18)$$

here $h_{\alpha}^{i,\text{eq}} = \phi_i \Gamma_{\alpha}$, where Γ_{α} is the dimensionless distribution function defined by

$$\Gamma_{\alpha} = w_{\alpha} \left[1 + \frac{\mathbf{e}_{\alpha} \cdot \mathbf{u}}{c_s^2} + \frac{(\mathbf{e}_{\alpha} \cdot \mathbf{u})^2}{2c_s^4} - \frac{\mathbf{u} \cdot \mathbf{u}}{2c_s^2} \right], \quad (19)$$

Where $c_s = c/\sqrt{3}$ is the lattice speed of sound. For D2Q9 lattice structure, $w_0 = 4/9$, $w_{1-4} = 1/9$ and $w_{5-8} = 1/36$. \mathbf{e}_{α} is the mesoscopic velocity:

$$\mathbf{e}_{\alpha} = c \begin{cases} (0, 0), & \alpha = 0 \\ (\cos \theta_{\alpha}, \sin \theta_{\alpha}), & \theta_{\alpha} = (\alpha - 1)\pi/2, \quad \alpha = 1 - 4 \\ (\cos \theta_{\alpha}, \sin \theta_{\alpha})\sqrt{2}, & \theta_{\alpha} = (2\alpha - 9)\pi/4, \quad \alpha = 5 - 8 \end{cases}, \quad (20)$$

where $c = \frac{\delta x}{\delta t}$, and δx and δt are the lattice length and timescale, respectively. In this paper the common value of $\delta x = \delta t = 1$ lu (lattice units) is taken. The phase field relaxation time is a function of the mobility:

$$\tau_{\phi} = \frac{M}{c_s^2 \delta t}. \quad (21)$$

The forcing term, $F_{\alpha}^{\phi,i}$ for three-component systems is defined by [25]

$$F_{\alpha}^{\phi,i} = \frac{1}{3} \delta t w_{\alpha} \left\{ 2\mathbf{e}_{\alpha} \cdot \mathbf{n}_i |\nabla \phi_i|^{\text{eq}} - \sum_{j \neq i} \mathbf{e}_{\alpha} \cdot \mathbf{n}_j |\nabla \phi_j|^{\text{eq}} \right\}. \quad (22)$$

The phase field variables are equal to the zeroth moment of their corresponding phase field distribution function:

$$\phi_i = \sum_{\alpha} h_{\alpha}^i; \quad i = 1, 2, \quad (23)$$

where ϕ_i is updated after the streaming step. As mentioned earlier the third phase field is not an independent variable and

can be calculated by

$$\phi_3 = 1 - \phi_1 - \phi_2. \quad (24)$$

The gradient and Laplacian of ϕ_i are calculated using the following equations:

$$\nabla \phi_i = \frac{c}{c_s^2 \delta x} \sum_{\alpha} \mathbf{e}_{\alpha} w_{\alpha} \phi_i(\mathbf{x} + \mathbf{e}_{\alpha} \delta t, t), \quad (25)$$

$$\nabla^2 \phi_i = \frac{2c^2}{c_s^2 (\delta x)^2} \sum_{\alpha} w_{\alpha} [\phi_i(\mathbf{x} + \mathbf{e}_{\alpha} \delta t, t) - \phi_i(\mathbf{x}, t)]. \quad (26)$$

Using a linear interpolation, the density can be obtained as follows:

$$\rho = \sum_{i=1}^3 \rho_i \phi_i. \quad (27)$$

The gradient of density can either be calculated by an equation similar to Eq. (25) or by a linear interpolation in the form

$$\nabla \rho = \sum_{i=1}^3 \rho_i \nabla \phi_i. \quad (28)$$

The latter approach makes ϕ_i the only macroscopic variable in the interface tracking model. In this study, Eq. (28) is used to calculate the gradient of density.

C. Hydrodynamic formulation

In this paper, the method proposed by Fakhari *et al.* [26] is implemented to solve for the hydrodynamic properties, i.e. velocity field and pressure. An additional distribution function must be introduced, which is called the hydrodynamic distribution function, g_{α} . The LBE for hydrodynamics can then be written as [26]

$$g_{\alpha}(\mathbf{x} + \mathbf{e}_{\alpha} \delta t, t + \delta t) = g_{\alpha}(\mathbf{x}, t) + \Omega_{\alpha}(g_{\alpha}, \bar{g}_{\alpha}^{\text{eq}}) + F_{\alpha}(\mathbf{x}, t), \quad (29)$$

Where Ω_{α} is the collision operator. The hydrodynamic forcing term is equal to

$$F_{\alpha}(\mathbf{x}, t) = \delta t w_{\alpha} \frac{\mathbf{e}_{\alpha} \cdot \mathbf{F}}{\rho c_s^2}. \quad (30)$$

The equilibrium distribution function g_{α}^{eq} is defined as

$$g_{\alpha}^{\text{eq}} = (\bar{p} + \Gamma_{\alpha}) w_{\alpha}, \quad (31)$$

where $\bar{p} = p/\rho c_s^2$ and p is the pressure.

The hydrodynamic forcing term is written as

$$\mathbf{F} = \mathbf{F}_s + \mathbf{F}_b + \mathbf{F}_p + \mathbf{F}_{\mu}, \quad (32)$$

where \mathbf{F}_s and \mathbf{F}_b are the surface tension and body force, respectively. For the three-component system \mathbf{F}_s takes the form:

$$\mathbf{F}_s = \sum_{i=1}^3 \mu_i \nabla \phi_i, \quad (33)$$

where $\mathbf{F}_p = -\bar{p} c_s^2 \nabla \rho$ is the pressure force and $\mathbf{F}_{\mu} = -\nu [\nabla \mathbf{u} + (\nabla \mathbf{u})^T] \cdot \nabla \rho$ is the viscous force [26]. The kinematic

viscosity, ν is a function of hydrodynamic relaxation time, τ_h :

$$\nu = \tau_h c_s^2 \delta t. \quad (34)$$

The collision operator can take different forms. The most commonly used form is the single-relaxation-time (BGK) model. The BGK model is fast and easier to implement. However, when relaxation times are very small, it becomes numerically unstable. In this paper a more sophisticated method called the multirelaxation-time (MRT) has been employed which is more accurate and much more stable than the BGK model. The MRT collision operator is defined by

$$\Omega_{\alpha} = -\mathbf{M}^{-1} \widehat{\mathbf{S}} \mathbf{M} (g_{\alpha} - \bar{g}_{\alpha}^{\text{eq}}), \quad (35)$$

where \mathbf{M} is the orthogonal transformation matrix [32], and $\widehat{\mathbf{S}}$ is the diagonal relaxation matrix:

$$\widehat{\mathbf{S}} = \text{diag}(1, 1, 1, 1, 1, 1, 1, s_{\nu}, s_{\nu}),$$

$$s_{\nu} = \frac{1}{\tau_h + 1/2}. \quad (36)$$

For the MRT collision operator, the viscous forcing term can be rewritten as

$$F_{\mu,i} = -\frac{\nu}{c_s^2 \delta t} \left\{ \sum_{\beta} e_{\beta i} e_{\beta j} \sum_{\alpha} (\mathbf{M}^{-1} \widehat{\mathbf{S}} \mathbf{M})_{\beta \alpha} (g_{\alpha} - g_{\alpha}^{\text{eq}}) \right\} \frac{\partial \rho}{\partial x_j};$$

$$i \in x, y. \quad (37)$$

The hydrodynamic relaxation time in each time step is calculated by a combination of a step function and a linear interpolation, which takes the following form:

$$\text{if } \phi_i > 0.99; i = 1, 2, 3 \quad \tau_h = \tau_i,$$

$$\text{otherwise } \tau_h = \tau_1 \phi_1 + \tau_2 \phi_2 + \tau_3 \phi_3, \quad (38)$$

where ϕ_g and ϕ_l are the gas and liquid phase field variables, respectively. This formulation maintains the relaxation time in the bulk of each phase and negates the effect of dispersion errors [25]. Another benefit of this formulation is that there is no need to update the collision operator in each time step in the bulk of each phase, which reduces CPU time.

The hydrodynamic properties are obtained by

$$\mathbf{u} = \sum_{\alpha} g_{\alpha} \mathbf{e}_{\alpha} + \frac{\mathbf{F}}{2\rho} \delta t, \quad (39)$$

$$\bar{p} = \sum_{\alpha} g_{\alpha}, \quad (40)$$

The LBE for hydrodynamics recovers the continuity and momentum equations for incompressible multicomponent flows:

$$\nabla \cdot \mathbf{u} = 0, \quad (41)$$

$$\frac{\partial \mathbf{u}}{\partial t} + \mathbf{u} \cdot \nabla \mathbf{u} = -\frac{\nabla p}{\rho} + \nabla \cdot \{ \nu [\nabla \mathbf{u} + (\nabla \mathbf{u})^T] \} + \frac{\mathbf{F}_s + \mathbf{F}_b}{\rho}. \quad (42)$$

D. Boundary conditions

According to Young's law, the equilibrium contact angle between the liquid-gas interface and the solid surface is

$$\cos \theta^{\text{eq}} = \frac{\sigma_{sg} - \sigma_{sl}}{\sigma_{lg}}, \quad (43)$$

where σ_{sg} , σ_{sl} and σ_{lg} are the solid-gas, solid-liquid, and liquid-gas interfacial tensions, respectively. At wall nodes if no solid-fluid interaction is present, Neumann boundary condition is applied, which takes the form of $\mathbf{n}_s \cdot \nabla \phi_i|_{x_s} = 0$. \mathbf{n}_s is the unit vector normal to the solid surface. This equation imposes the no-flux condition at the boundaries. If a fluid-fluid interface is present at a wall node, the contact angle on the solid surface can be specified by

$$\mathbf{n}_s \cdot \nabla \phi_i|_{x_s} = \frac{4}{\xi} \Omega_\theta \phi_s (1 - \phi_s), \quad (44)$$

where Ω_θ is related to the equilibrium contact angle θ^{eq} by $\Omega_\theta = -\cos \theta^{\text{eq}}$ and ϕ_s is the phase field variable on the solid wall. For more details on numerical implementation of Eq. (44) refer to Ref. [33]. Note that for a three-component system the condition is only imposed for two of the components and the third phase field variable is given by Eq. (24).

E. Numerical validation

In this section we check the accuracy of the numerical method by measuring the maximum droplet height for different equilibrium contact angles of liquid droplet on a flat substrate and comparing them with theoretical values. The theoretical droplet height for a given equilibrium contact angle is [33]

$$\frac{h_m}{r} = (1 - \cos \theta^{\text{eq}}) \sqrt{\frac{\pi}{2\theta - \sin 2\theta^{\text{eq}}}}. \quad (45)$$

A droplet is placed on a flat substrate with an initial contact angle of 90° . Simulations are performed for different θ^{eq} until equilibrium is reached. Three different equilibrium states are demonstrated in Fig. 1. Figure 2 shows the comparison between the numerical result and the theory [Eq. (45)].

To verify the accuracy of flow dynamics in the numerical model, the capillary rise of liquid in a vertical tube is simulated and compared with the Lucas-Washburn (L-W) law. According to Lucas and Washburn [34,35], the height of the liquid column, h_{cap} is given by

$$h_{\text{cap}} = \frac{\sigma_{lg} R_t \cos \theta}{2\mu} t. \quad (46)$$

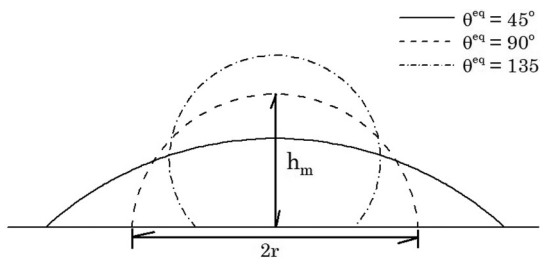


FIG. 1. Different equilibrium states for a droplet with an initial contact angle of 90° ; the lines represent $\phi_1 = 0.5$.

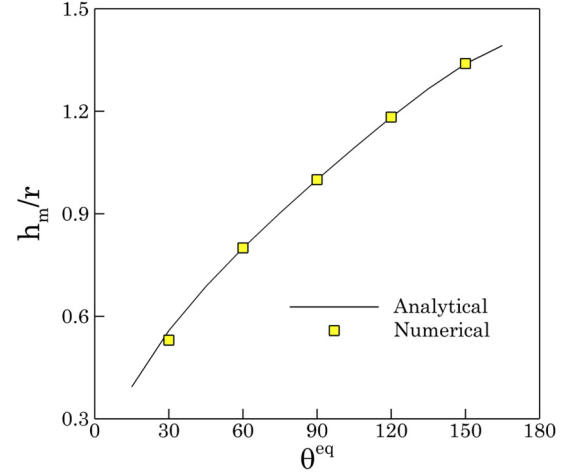


FIG. 2. Simulated and analytical dimensionless droplet height for different equilibrium contact angles. The solid black line shows the theory [Eq. (45)], and the square symbols show the simulation results.

The radius of the tube is denoted by R_t . Since the gravity effects are neglected in L-W law, we run the simulation with $g = 0$. The LBM tube radius is $R_{t,\text{LBM}} = 5 \text{ lu}$ and the time is scaled by the viscous timescale, $\tau_v = \rho_l R_t^2 \eta^{-1}$ [36]. As shown in Fig. 3, there is a significant difference between the LBM results and L-W law. This difference, which can also be seen in experimental results [37], is due to initial inertial effects, which are not included in the L-W law. However, during the second stage where the flow is dominated by capillary and viscous effects, the LBM predicted height matches the theoretical height.

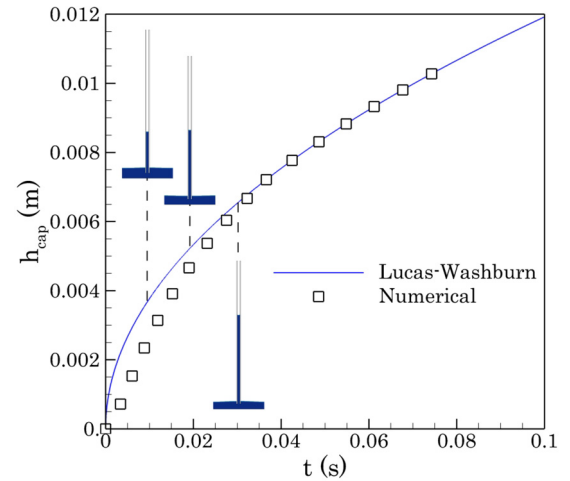


FIG. 3. Capillary rise of liquid under zero gravity condition. The solid line shows the theoretical height given by the Lucas-Washburn equation, and the obtained numerical height is shown by square symbols. $R_t = 0.1 \text{ mm}$, $\theta^{\text{eq}} = 47^\circ$, $\eta_l = 6 \times 10^{-4} \text{ Pa} \cdot \text{s}$, $\rho_l = 750 \text{ kg} \cdot \text{m}^{-3}$, $\sigma_{lg} = 2.5 \times 10^{-3} \text{ N} \cdot \text{m}^{-1}$. l denotes the liquid properties.

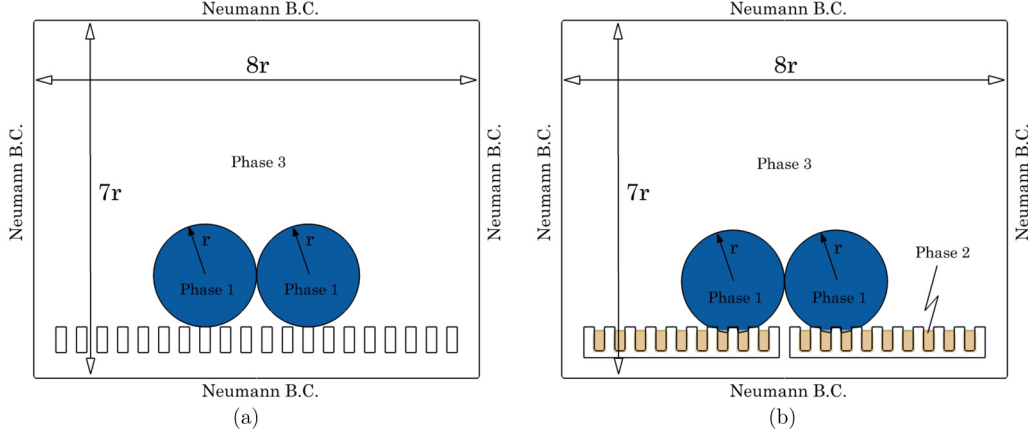


FIG. 4. Schematic of the problem setup for (a) two-phase system and (b) three-phase system.

IV. PROBLEM DESCRIPTION

The simulation setup as shown in Fig. 4 consists of two identical water droplets (phase 1) sitting on top of the substrate. The droplets are initially close enough to each other so that the liquid bridge can form between them. The substrate has rectangular micropillars and the space between the pillars is filled with a liquid which is immiscible with water (phase 2). The gas (phase 3) is assumed to be atmospheric air.

In 2D simulations, during coalescence the air gets trapped in the space under the liquid bridge with nowhere to escape. The pressure of the trapped air increases as it is pushed by the droplets towards the substrate. This increase in pressure can significantly affect the jumping process and lead to discrepancy between 2D and 3D results. Also in three-phase systems, it might cause numerical instability. To solve this issue for the three-phase system, we remove the substrate underneath the space between the two center pillars so that the air can escape. For the water-air system, we remove the entire substrate underneath the pillars [Fig. 4(a)]. Since the droplets are in Cassie state, they don't make contact with the lower portion of the pillars.

Neumann boundary condition is applied to the outer boundaries of the domain. On account of the small size of the droplets, the gravity effects are neglected. The important parameters in this study are listed in Table I in dimensionless form.

TABLE I. List of parameters.

Parameter	Value
Water-air dynamic viscosity ratio, η_1^*	55
Water-air density ratio, ρ_1^*	800
Lubricant-air dynamic viscosity ratio, η_2^*	55
Lubricant-air density ratio, ρ_2^*	800
Pillar width-droplet radius, w_p/r	1/5
Pillar-to-pillar distance-droplet radius, d_p/r	1/5
Pillar height-droplet radius, h_p/r	1/2
Solid-water equilibrium contact angle, θ_1^{eq}	160°
Solid-lubricant equilibrium contact angle, θ_2^{eq}	100°

The y-component of the dimensionless droplet velocity is calculated by

$$U_j^* = \frac{\int_{\Omega} \rho_1 U^* dV}{\int_{\Omega} \rho_1 dV}, \quad (47)$$

where $U^* = u_y/U_{ic}$. In order to evaluate the grid dependency of the results, the maximum jumping velocity for the water-air system has been obtained for different lattice droplet radii. Table II shows the results of the simulations. Since the difference in jumping velocity between $r_l = 30$ lu and $r_l = 40$ lu is small, we set the droplet radius to 30 lu.

V. RESULTS AND DISCUSSION

In this section, the results of the numerical simulations are presented. In the first subsection, the jumping process in the two-phase system is investigated. The effects of several parameters on the jumping process is studied for the three-phase system in the next subsections. Finally a comparison between the two cases is presented.

A. Water-air system

The time evolution of droplets for $\theta_1^{\text{eq}} = 160^\circ$ and $\text{Oh} = 0.017$ is demonstrated in Fig. 5. The time is nondimensionalized by $t^* = t/\tau$ where $\tau = \sqrt{\rho r^3/\sigma_{13}}$. The jumping process consists of four distinct stages [38]. The first stage is the formation and expansion of the capillary bridge between the droplets ($t^* = 0.5$). The second stage starts when the capillary bridge hits the micropillars, which creates a force that accelerates the coalesced droplet upward ($t^* = 1$). If the momentum built during the second stage overcomes wall adhesion, the

TABLE II. Grid dependency test for water-air system with $\theta_1^{\text{eq}} = 160^\circ$, $\rho_1^* = 800$, $\eta_1^* = 55$, and $\text{Oh} = 0.017$.

Lattice droplet radius, r_l	Dimensionless jumping velocity, U_j^*
20 lu	0.311
30 lu	0.302
40 lu	0.299

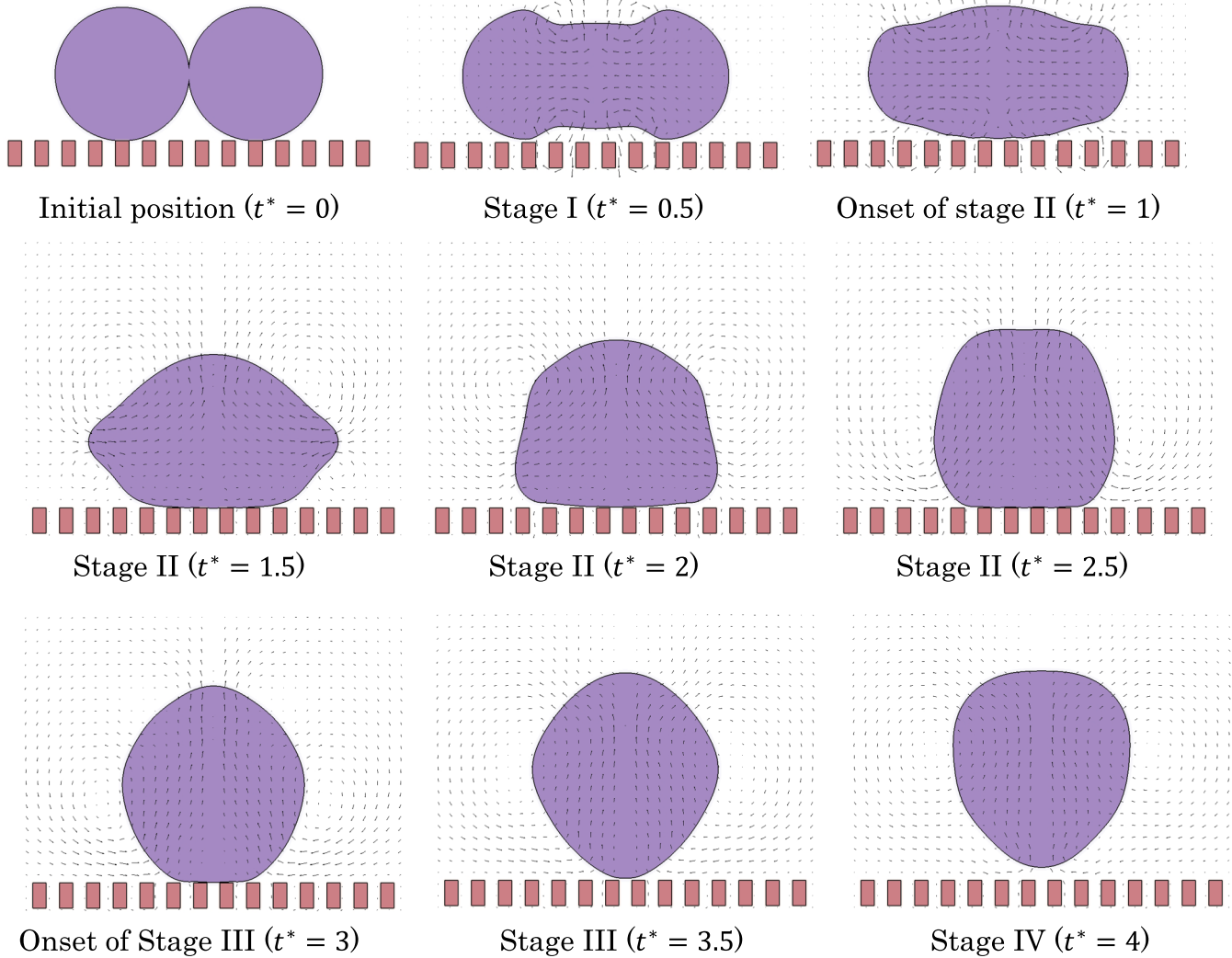


FIG. 5. Time evolution of coalescence-induced droplet jumping for the water-air system, $\theta_1^{\text{eq}} = 160^\circ$ and $\text{Oh} = 0.017$.

droplet will detach from the surface, which is called the third stage ($t^* = 3.5$). At the fourth stage the departed droplet will decelerate due to air friction and gravity effects ($t^* > 4$).

The jumping velocity of the droplet immediately after departure is plotted versus the initial droplet radius for $\theta_1^{\text{eq}} = 160^\circ$, and is compared against theoretical and experimental values in Fig. 6(a). The theoretical jumping velocity is taken as $U_{j,\text{th}} = 0.23U_{ic}$ and the experimental data are obtained by Kim *et al.* [10] on a low-adhesion surface.

The theory assumes that the efficiency of energy conversion during coalescence is constant for all droplet sizes. Hence, the theoretical jumping velocity tends to infinity as the droplet size is decreased. However, this assumption is not correct. Figure 6(b) demonstrates the dimensionless jumping velocity for different initial droplet radii. The numerical results show that for bigger droplets the dimensionless jumping velocity is larger. This is due to the fact that viscous dissipation plays a smaller role compared to inertial-capillary forces

for bigger droplets. This explains the discrepancy between the theory and the numerical results.

According to Fig. 6(a), the jumping velocity is larger for smaller droplets. This is simply due to the lower mass of droplets, which gives them better acceleration during the third stage of the jumping process. However, for very small droplets ($r < 3 \mu\text{m}$) in the numerical simulations and experimental data, the energy conversion efficiency is very low, and as a result the jumping velocity decreases. Therefore, there exist a radius for which the jumping velocity is maximum.

B. Water-lubricant-air system

The time evolution of the jumping process for $\text{Oh} = 0.017$, $\sigma_{12}^* = 0.75$, and $\sigma_{23}^* = 0.4$ is shown in Fig. 7. The dimensionless lubricant surface tension and water-lubricant interfacial tension are defined as $\sigma_{23}^* = \sigma_{23}/\sigma_{13}$ and $\sigma_{12}^* = \sigma_{12}/\sigma_{13}$, respectively.

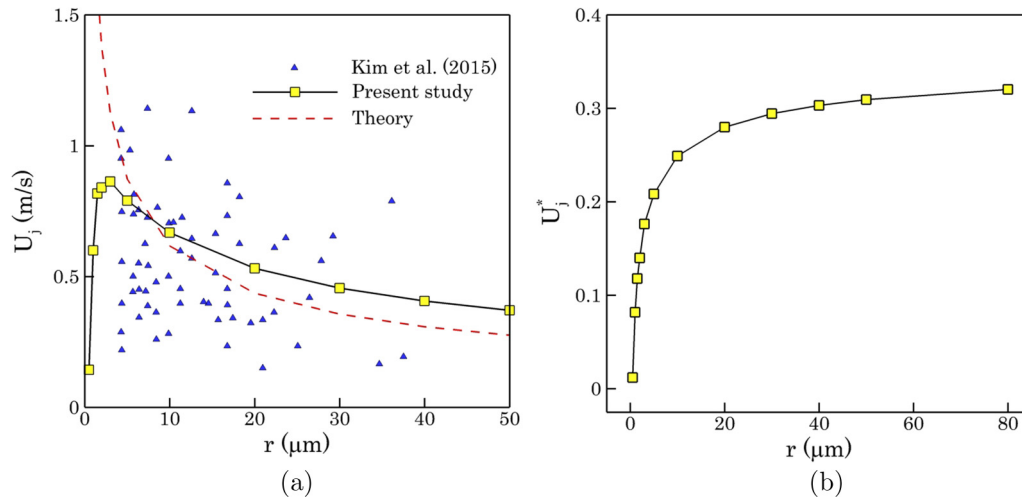


FIG. 6. (a) Droplet jumping velocity as a function of initial droplet radius. The numerical result is shown by the solid line with square symbols, the triangles represent the experimental results by Ref. [10], and the dashed line is the theoretical value. (b) Dimensionless droplet jumping velocity as a function of initial droplet radius.

According to Fig. 8 the jumping process (starting from coalescence up to droplet departure point) can be divided into five distinct stages. Similar to the water-air system, in stage I the capillary liquid bridge begins to form and grow ($t^* = 0.2$). But due to the adhesion between the water droplets and the lubricant, a downward force accelerates the droplets towards the substrate. During stage II, the capillary bridge

hits the micropillars ($t^* = 0.57$). This exerts an upward force on the droplets. At this time, the capillary-induced upward force is greater than the water-lubricant adhesion force and the droplets are accelerated away from the micropillars. The droplet velocity remains constant for a brief period of time at stage III ($t^* = 1$). Then the droplet continues to accelerate away from the surface during stage IV ($t^* = 1.4$). Stage V is

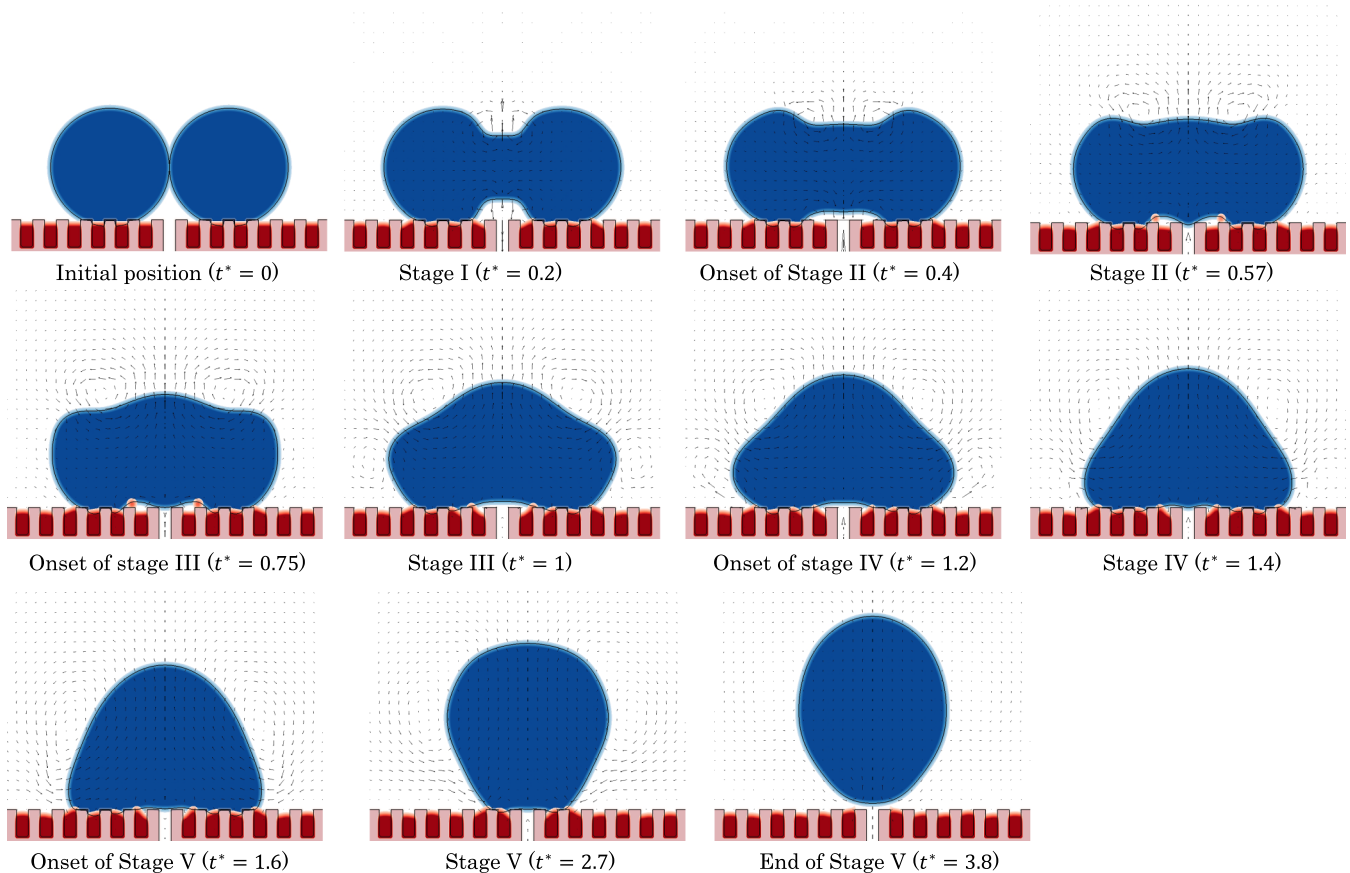


FIG. 7. Snapshots of droplet shape evolution in water-lubricant-air system for $\sigma_{12}^* = 0.75$ and $\sigma_{23}^* = 0.4$.

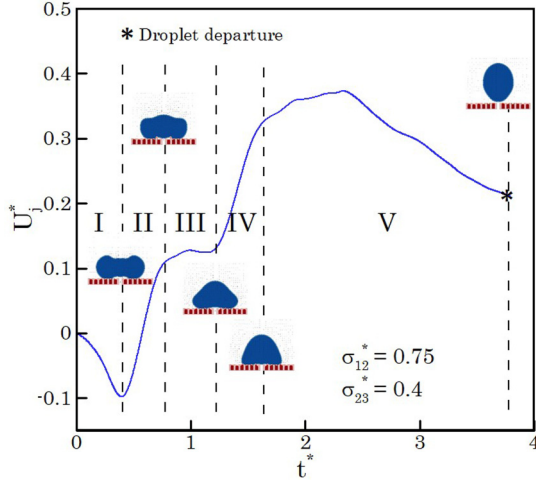


FIG. 8. Time evolution of the dimensionless droplet velocity and stages of the jumping process before departure in the three-phase system for $\sigma_{12}^* = 0.75$ and $\sigma_{23}^* = 0.4$.

similar to the third stage in the water-air system, where the merged droplet begins detaching from the surface ($t^* = 2.7$). As mentioned earlier, during the coalescence process, gravity effects are very small. However after droplet departure, gravity is an important factor in determining the jumping height of the droplet.

1. The effect of lubricant surface tension

An important factor that affects droplet coalescence in three-phase systems is the surface tension of the lubricant. Two surface related parameters of the lubricant are the dimensionless lubricant surface tension, σ_{23}^* and the water-lubricant interfacial tension σ_{12}^* . Here we perform two sets of simulations. In the first case, the lubricant surface tension is constant: $\sigma_{23}^* = 0.4$ and σ_{12}^* is changed from 0.7 to 0.95. In the second case $\sigma_{12}^* = 0.9$ and σ_{23}^* varies from 0.4 to 0.7.

Figures 9 and 10 show the time evolution of dimensionless droplet velocity for $Oh = 0.017$ for cases 1 and 2,

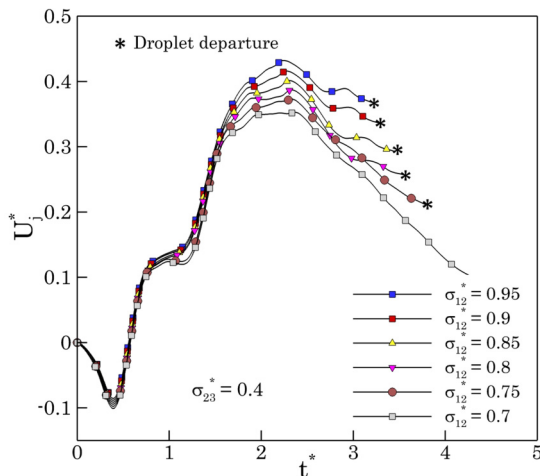


FIG. 9. Dimensionless droplet velocity in the three-phase system for $\sigma_{23}^* = 0.4$ and $\sigma_{12}^* = 0.7-0.95$.

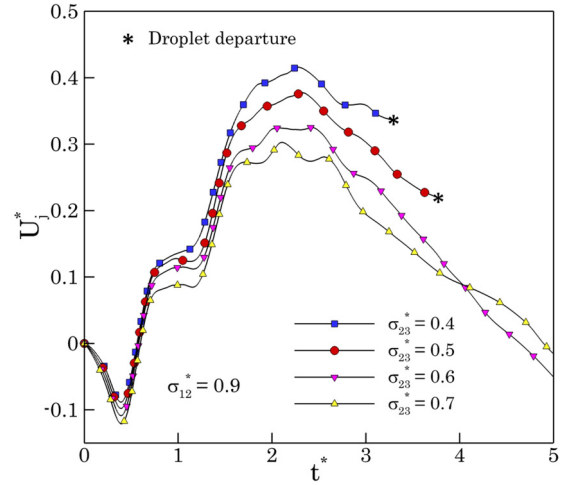


FIG. 10. Dimensionless droplet velocity in the three-phase system for $\sigma_{12}^* = 0.9$ and $\sigma_{23}^* = 0.4-0.7$.

respectively. Changing σ_{23}^* and σ_{12}^* does not have a major effect on the first four stages. However in stage V where the merged droplet start to detach, the effect becomes noticeable. Increasing σ_{12}^* and decreasing σ_{23}^* enhances the dimensionless jumping velocity significantly. For relatively low σ_{12}^* (<0.75) and high σ_{23}^* values (>0.5) jumping does not occur. This can be explained by a parameter called the spreading coefficient, S_i which is defined as [39]

$$S_i = -\gamma_i = \sigma_{jk} - \sigma_{ij} - \sigma_{ik}. \quad (48)$$

This parameter is different from the work of adhesion [Eq. (3)]. For a partially spread system, the spreading coefficient is negative and the less negative it is the greater the tendency of phase i is to be spread over the jk interface [39].

In this case, the spreading coefficient of the water droplets, $S_1 = \sigma_{23} - \sigma_{12} - \sigma_{13}$ becomes more negative as σ_{12}^* increases and σ_{23}^* decreases. Therefore the tendency of water droplets to be spread over the lubricant-air interface reduces. According to Eq. (4) the work of adhesion also decreases, which leads to an increase in the jumping velocity.

2. The effect of initial droplet radius

The initial size of the droplets is a key parameter in the jumping process [6,9]. Figure 11 shows the temporal evolution of dimensionless droplet velocity for different initial droplet radii. The droplet radius is varied from $r = 5 \mu\text{m}$ ($Oh = 0.053$) to $50 \mu\text{m}$ ($Oh = 0.017$). As mentioned earlier, the viscous effects are larger for smaller droplets. Therefore, the jumping velocity decreases. Also the dimensionless departure time is longer for smaller droplets.

The dimensionless jumping velocity as a function of initial droplet radius for different interfacial tensions is illustrated in Fig. 12. For droplets smaller than the critical jumping radius, jumping does not occur due to larger viscous effects. According to Fig. 12 the critical jumping radius is smaller for higher lubricant-water interfacial tensions.

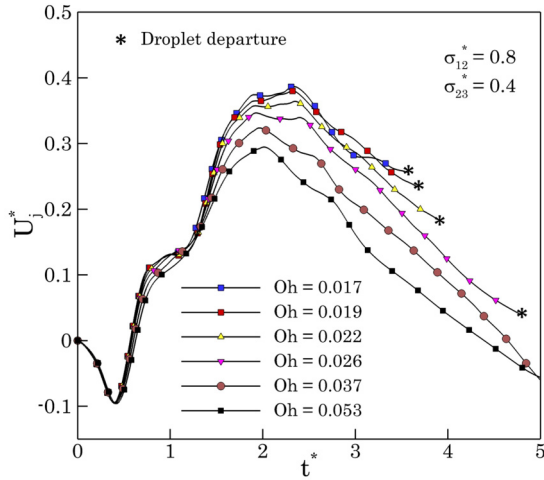


FIG. 11. Effect of initial droplet radius on dimensionless droplet jumping velocity in the three-phase system for $\sigma_{12}^* = 0.8$ and $\sigma_{23}^* = 0.4$.

3. Surface wettability effects

An important parameter that affects droplet mobility is the solid surface adhesion which can be quantified in terms of the equilibrium contact angle. Here we perform simulations for different contact angles between the water droplets and the solid surface. The results of the simulation can be seen in Fig. 13. A higher contact angle means there is less surface adhesion. As a result, the droplet becomes more mobile and jumping velocity increases. There exist a critical contact angle for which jumping does not occur. The critical contact angle for a micropillar substrate without lubricant has been shown to be $\theta_c^{eq} \approx 120^\circ$ [21]. According to Fig. 13 the cutoff is much higher for lubricant-infused surfaces ($\theta_c^{eq} \approx 150^\circ$).

It is important to note that currently the maximum achievable contact angle on smooth liquid-infused surfaces is roughly 118° which is much lower than the calculated cutoff value of 150° [40]. Therefore, the objective of this study is not necessarily to replicate the realistic conditions, but to explore the extremities in order to find a better understanding of the

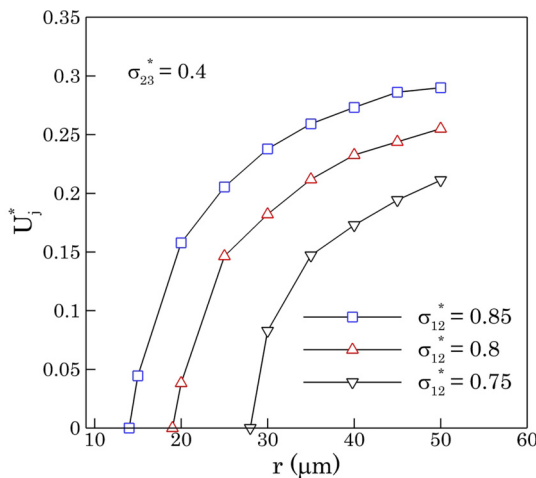


FIG. 12. Dimensionless droplet jumping velocity as a function of initial droplet radius for the three-phase system.

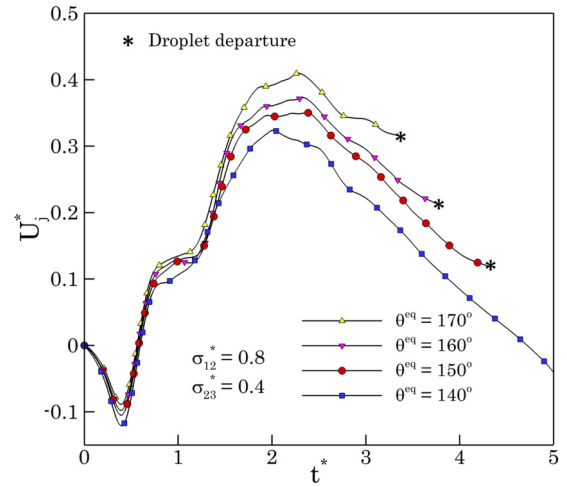


FIG. 13. The effect of surface wettability on jumping velocity at $Oh = 0.017$. The surface wettability is quantified by specifying the equilibrium contact angle θ^{eq} , which is varied from 140° to 170° .

underlying mechanisms involved in droplet coalescence on such surfaces.

4. Lubricant viscosity effects

In this case, the dynamic viscosity of the lubricant is varied, in order to study the effects of the viscosity ratio on the droplet jumping velocity. The densities are equal ($\rho_1 = \rho_2$) and $Oh = 0.017$. As demonstrated by Fig. 14 the jumping velocity is not a function of the lubricant dynamic viscosity. Therefore, at the lubricant-water interface, the viscous forces are less important compared to the interfacial tension forces.

C. Comparison between two-phase and three-phase systems

If we overlay the results of two-phase and three-phase systems, we can see the difference in the jumping process between the two cases. Figure 15 shows a comparison between the two cases at different stages. During the early stages, the droplet velocity stays almost constant in the water-air system,

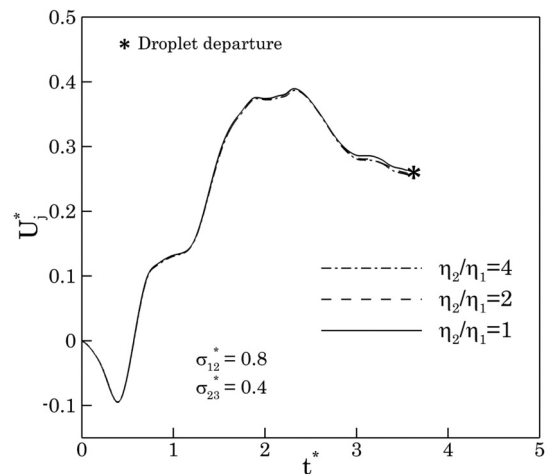


FIG. 14. The effect of lubricant viscosity on jumping velocity of the merged droplet.

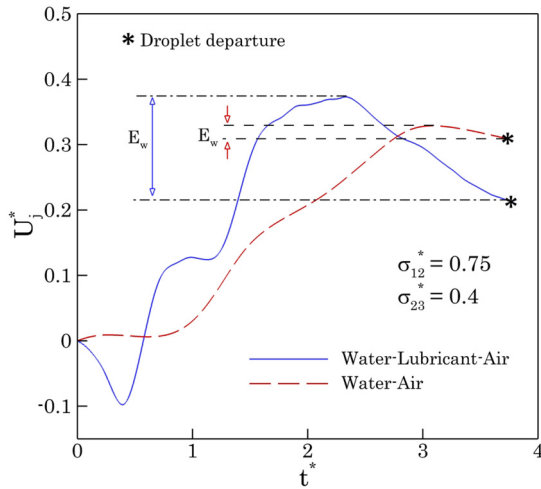


FIG. 15. Dimensionless droplet velocity U_j^* , comparison between two-phase and three-phase systems. U_j^* is shown by the solid line for the three-phase systems, and for the two-phase system is shown by the dashed line. The work of adhesion is also shown for the two cases.

but in the three-phase system there is a dip in droplet velocity, which is due to the adhesion forces between the lubricant and the water droplets. In the next stage, the y -component momentum growth rate is greater for the three-phase system. This growth rate is much smoother in the absence of the lubricant. Figure 16 compares the velocity field for the two systems. During the departure stage, the maximum merged droplet velocity prior to detachment is higher for the three-phase system, and is also achieved at an earlier time. This might be due to the lubricant acting like a flat surface at this stage of the jumping process. It has been shown that for the same surface wettability, on a flat surface the maximum achievable velocity prior to detachment is higher compared to a patterned surface [21]. Since the contact area between the solid and the droplet is bigger for flat surfaces, the upward force is also larger, which explains the higher maximum velocity for the three-phase system. However due to higher adhesion forces, kinetic energy loss is higher when lubricant is present, and consequently the jumping velocity is lower. The droplet departure time is almost identical between the two cases.

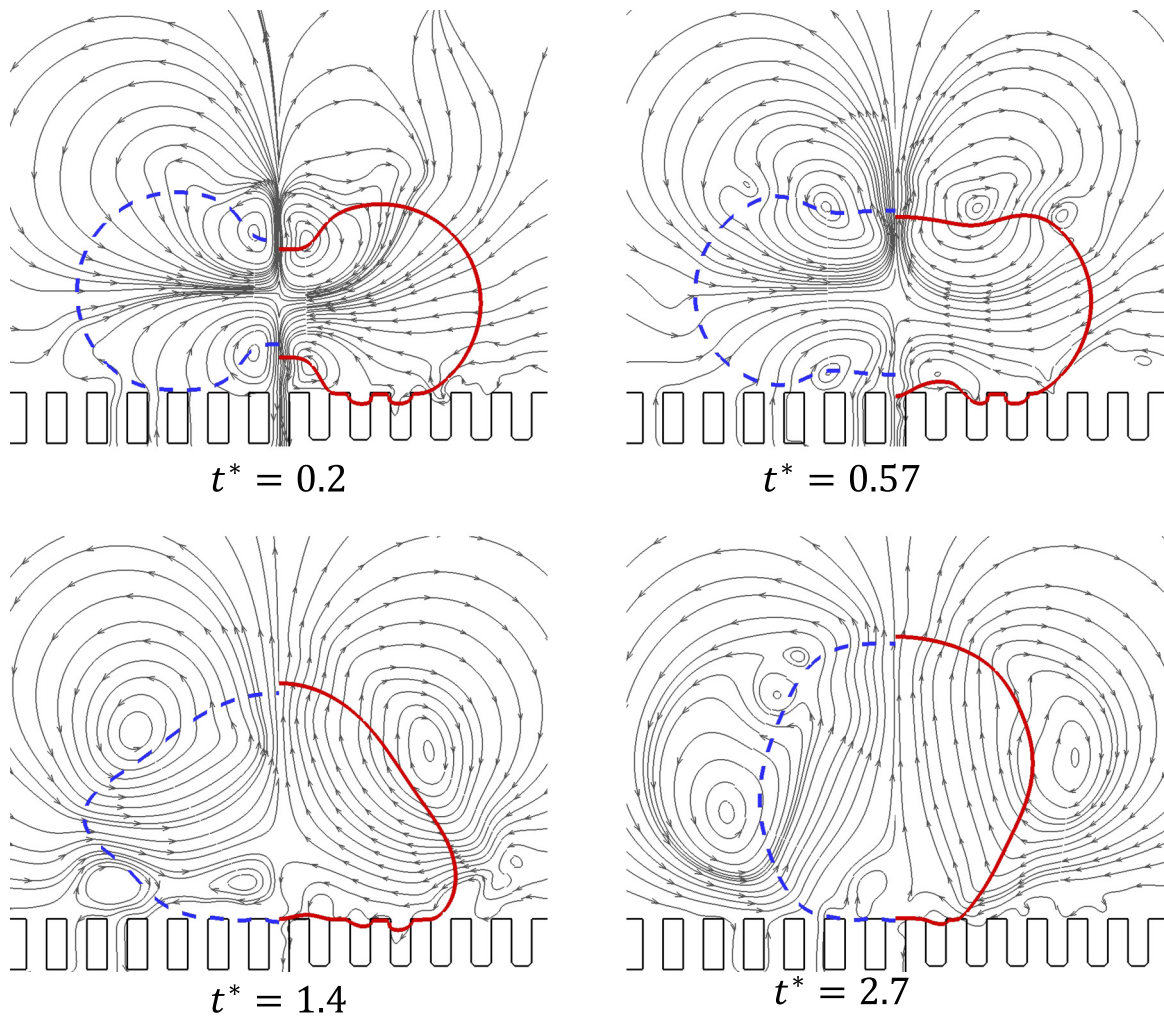


FIG. 16. Velocity field in two-phase and three-phase systems. The two-phase and three-phase systems are shown in the left and right halves of each frame, respectively. The dotted blue line is the droplet shape in the two-phase, and the solid red is for the three-phase system. The lines represent $\phi_1 = 0.5$.

It has to be mentioned that for some cases, where the spreading coefficient is algebraically small (more negative), the jumping velocity becomes greater than that of the water-air system. This is due to the very low tendency of the droplets to be spread over the lubricant-air interface. As a result, the lubricant-water adhesion becomes smaller than the water-solid adhesion forces, which leads to higher jumping velocities for very small spreading coefficients.

VI. CONCLUSION

In this paper, the coalescence-induced droplet jumping phenomenon on pillared surfaces in a three-phase system was studied. A recently developed mass-conserving LBM for multiphase flows was employed to numerically solve the problem. The effects of several parameters, such as surface and interfacial tensions, initial droplet size, surface wettability and density ratio on the dimensionless jumping velocity was investigated and compared with the results obtained for regular pillared surfaces. The results demonstrated that surface

tension and interfacial tension are key parameters in the jumping process. For higher water-lubricant interfacial tensions and lower lubricant surface tensions, the jumping velocity was found to be higher. This is due to the lower tendency of droplets to be spread over the lubricant-air interface, which lowers the kinetic energy loss due to interfacial adhesion forces. The initial droplet size is another important parameter in determining whether droplet detachment can happen. The results show that the critical jumping radius is highly dependent on surface parameters and is smaller for higher water-lubricant interfacial tensions. The surface wettability effects was also studied. The minimum contact angle for which the merged droplet is capable of detaching is $\sim 150^\circ$ in three-phase systems, which is much higher than $\sim 120^\circ$ for a two-phase system. Also, numerical simulations demonstrate that the water-lubricant viscosity ratio does not have a noticeable impact on the jumping process, signifying that the viscous effects at the water-lubricant interface are a less important factor compared to adhesion forces in coalescence-induced droplet jumping in three-phase systems.

-
- [1] K. M. Wisdom, J. A. Watson, F. Liu, G. S. Watson, and C. H. Chen, Self-cleaning of super-hydrophobic surfaces by self-propelled jumping condensate, *Proc. Natl. Acad. Sci. USA* **110**, 7992 (2013).
 - [2] G. S. Watson, M. Gellender, and J. A. Watson, Self-propulsion of dew drops on lotus leaves: A potential mechanism for self-cleaning, *Biofouling* **30**, 427 (2014).
 - [3] K. Rykaczewski, A. T. Paxson, S. Anand, X. Chen, Z. Wang, and K. K. Varanasi, Multimode multidrop serial coalescence effects during condensation on hierarchical superhydrophobic surfaces, *Langmuir* **29**, 881 (2013).
 - [4] N. Miljkovic, R. Enright, Y. Nam, K. Lopez, N. Dou, J. Sack, and E. N. Wang, Jumping-droplet-enhanced condensation on scalable super-hydrophobic nanostructured surfaces, *Nano Lett.* **13**, 179 (2012).
 - [5] K. Yanagisawa, M. Sakai, T. Isobe, S. Matsushita, and A. Nakajima, Investigation of droplet jumping on superhydrophobic coatings during dew condensation by the observation from two directions, *Appl. Surf. Sci.* **315**, 212 (2014).
 - [6] J. B. Boreyko and C. H. Chen, Self-Propelled Dropwise Condensate on Super Hydrophobic Surfaces, *Phys. Rev. Lett.* **103**, 184501 (2009).
 - [7] J. B. Boreyko and C. P. Collier, Delayed frost growth on jumping-drop superhydrophobic surfaces, *ACS Nano* **7**, 1618 (2013).
 - [8] M. Kollera and U. Grigull, Über das Abspringen von Tropfen bei der Kondensation von Quecksilber, *Wärme- Stoffübertrag.* **2**, 31 (1969).
 - [9] R. Enright, N. Miljkovic, J. Sprittles, K. Nolan, R. Mitchell, and E. N. Wang, How coalescing droplets jump, *ACS Nano* **8**, 10352 (2014).
 - [10] M. K. Kim, H. Cha, P. Birbarah, S. Chavan, C. Zhong, Y. Xu, and N. Miljkovic, Enhanced jumping-droplet departure, *Langmuir* **31**, 13452 (2015).
 - [11] X. Chen, R. S. Patel, J. A. Weibel, and S. V. Garimella, Coalescence-induced jumping of multiple condensate droplets on hierarchical superhydrophobic surfaces, *Sci. Rep.* **6**, 18649 (2016).
 - [12] H. Cha, J. M. Chun, J. Sotelo, and N. Miljkovic, Focal plane shift imaging for the analysis of dynamic wetting processes, *ACS Nano* **10**, 8223 (2016).
 - [13] C. Lv, P. Hao, Z. Yao, and F. Niu, Departure of condensation droplets on superhydrophobic surfaces, *Langmuir* **31**, 2414 (2015).
 - [14] Z. Liang and P. Keblinski, Coalescence-induced jumping of nanoscale droplets on super-hydrophobic surfaces, *Appl. Phys. Lett.* **107**, 143105 (2015).
 - [15] K. Wang, R. Li, Q. Liang, R. Jiang, Y. Zheng, Z. Lan, and X. Ma, Critical size ratio for coalescence-induced droplet jumping on superhydrophobic surfaces, *Appl. Phys. Lett.* **111**, 061603 (2017).
 - [16] S. Farokhirad, J. F. Morris, and T. Lee, Coalescence-induced jumping of droplet: Inertia and viscosity effects, *Phys. Fluids* **27**, 102102 (2015).
 - [17] Y. Cheng, J. Xu, and Y. Sui, Numerical investigation of coalescence-induced droplet jumping on superhydrophobic surfaces for efficient dropwise condensation heat transfer, *Int. J. Heat Mass Transfer* **95**, 506 (2016).
 - [18] R. Attarzadeh and A. Dolatabadi, Coalescence-induced jumping of micro-droplets on heterogeneous superhydrophobic surfaces, *Phys. Fluids* **29**, 012104 (2017).
 - [19] X. Liu and P. Cheng, 3D multiphase lattice Boltzmann simulations for morphological effects on self-propelled jumping of droplets on textured superhydrophobic surfaces, *Int. Commun. Heat Mass Transfer* **64**, 7 (2015).
 - [20] X. Liu, P. Cheng, and X. Quan, Lattice Boltzmann simulations for self-propelled jumping of droplets after coalescence on a superhydrophobic surface, *Int. J. Heat Mass Transfer* **73**, 195 (2014).
 - [21] S. Farokhirad, M. M. Shad, and T. Lee, Coalescence-induced jumping of immersed and suspended droplets on microstructured substrates, *Eur. J. Comput. Mech.* **26**, 205 (2017).

- [22] T. Lee and L. Liu, Lattice Boltzmann simulations of micron-scale drop impact on dry surfaces, *J. Comput. Phys.* **229**, 8045 (2010).
- [23] J. Wasserfall, P. Figueiredo, R. Kneer, W. Rohlf, and P. Pischke, Coalescence-induced droplet jumping on superhydrophobic surfaces: Effects of droplet mismatch. *Phys. Rev. Fluids* **2**, 123601 (2017).
- [24] M. Geier, A. Fakhari, and T. Lee, Conservative phase-field lattice Boltzmann model for interface tracking equation, *Phys. Rev. E* **91**, 063309 (2015).
- [25] R. H. H. Abadi, M. H. Rahimian, and A. Fakhari, Conservative phase-field lattice-Boltzmann model for ternary fluids, *J. Comput. Phys.* **374**, 668 (2018).
- [26] A. Fakhari, T. Mitchell, C. Leonardi, and D. Bolster, Improved locality of the phase-field lattice-Boltzmann model for immiscible fluids at high density ratios, *Phys. Rev. E* **96**, 053301 (2017).
- [27] C. Lv, P. Hao, Z. Yao, Y. Song, X. Zhang, and F. He, Condensation and jumping relay of droplets on lotus leaf, *Appl. Phys. Lett.* **103**, 021601 (2013).
- [28] J. N. Israelachvili, *Intermolecular and Surface Forces*, 3rd ed. (Academic Press, Boston, 2011).
- [29] J. Eggers, J. R. Lister, and H. A. Stone, Coalescence of liquid drops, *J. Fluid Mech.* **401**, 293 (1999).
- [30] L. Duchemin, J. Eggers, and C. Josserand, Inviscid coalescence of drops, *J. Fluid Mech.* **487**, 167 (2003).
- [31] F. Boyer and C. Lapuerta, Study of a three component Cahn-Hilliard flow model, *ESAIM: Math. Model. Numer. Anal.* **40**, 653 (2006).
- [32] P. Lallemand and L.-S. Luo, Theory of the lattice Boltzmann method: Dispersion, dissipation, isotropy, Galilean invariance, and stability, *Phys. Rev. E* **61**, 6546 (2000).
- [33] A. Fakhari and D. Bolster, Diffuse interface modeling of three-phase contact line dynamics on curved boundaries: A lattice Boltzmann model for large density and viscosity ratios, *J. Comput. Phys.* **334**, 620 (2017).
- [34] R. Lucas, The time law of the capillary rise of liquids, *Kolloid Z.* **23**, 15 (1918).
- [35] E. W. Washburn, The dynamics of capillary flow, *Phys. Rev.* **17**, 273 (1921).
- [36] M. Stange, M. E. Dreyer, and H. J. Rath, Capillary driven flow in circular cylindrical tubes, *Phys. Fluids* **15**, 2587 (2003).
- [37] N. Ichikawa and Y. Satoda, Interface dynamics of capillary-flow in a tube under negligible gravity condition, *J. Colloid Interface Sci.* **162**, 350 (1994).
- [38] F. Liu, G. Ghigliotti, J. J. Feng, and C.-H. Chen, Numerical simulations of self-propelled jumping upon drop coalescence on non-wetting surfaces, *J. Fluid Mech.* **752**, 39 (2014).
- [39] J. S. Rowlinson and B. Widom, *Molecular Theory of Capillarity* (Clarendon Press, Oxford, 1982).
- [40] T.-S. Wong, S. H. Kang, S. K. Y. Tang, E. J. Smythe, B. D. Hatton, A. Grinthal, and J. Aizenberg, Bioinspired self-repairing slippery surfaces with pressure-stable omniphobicity, *Nature (London)* **477**, 443 (2011).